Original Article

On the chemical and microstructural requirements for the pesting-resistance of Mo–Si–Ti alloys

Susanne Obert[a], Alexander Kauffmann[a],*, Sascha Seils[a,b], Steven Schellert[c], Matthias Weber[c], Bronislava Gorr[c], Hans-Jürgen Christ[c], Martin Heilmaier[a]

[a] *Karlsruhe Institute of Technology (KIT), Institute for Applied Materials (IAM-WK), Engelbert-Arnold-Straße 4, 76131 Karlsruhe, Germany*
[b] *Karlsruhe Nano Micro Facility (KNMF), Karlsruhe Institute of Technology (KIT), Hermann-von-Helmholtz-Platz 1, 76344 Eggenstein-Leopoldshafen, Germany*
[c] *University of Siegen, Department of Mechanical Engineering, Paul-Bonatz-Straße 9-11, 57068 Siegen, Germany*

ARTICLE INFO

ABSTRACT

In recent publications [Schliephake et al. in Intermetallics 104 (2019) 133–142 and Obert, Kauffmann & Heilmaier in Acta Materialia, 184 (2020) 132–142], an unexpected pesting-stability of fully eutectic and specific eutectic–eutectoid Mo–Si–Ti alloys was found. Several potential reasons were proposed: microstructural length scale being typically very fine due to the eutectic and eutectoid reactions, the phase distribution including the fraction of the eutectic and eutectoid regions, as well as the chemical composition of the individual phases. In the present study, we prove the Ti content to be decisive for the pesting-resistance in air at 800 °C by investigating the microstructure and oxidation behaviour of Mo–Si–Ti alloys with systematically varying nominal Ti content. A critical Ti content of 43 at% was identified. Due to the phase equilibrium, this corresponds to a local Ti content in Mo solid solution of 35 at%. Other microstructural properties such as (i) lamellar size within eutectic and eutectoid regions and (ii) volume fraction of the eutectic and eutectoid regions were demonstrated to have an insignificant influence on the pesting-resistance of the alloys. Rather, the assessment of the oxidation behaviour of the monolithic phase Mo_{SS}, which was identified to be crucial for the oxidation behaviour of the Mo–Si–Ti alloys, confirmed an improvement in oxidation behaviour with increasing Ti content.

1. Introduction

Ti macro-alloyed Mo–Si-based alloys are attracting increasing attention as potential alternative materials for high temperature structural applications. Besides a high solidus temperature of about 1900 °C and, consequently, good creep resistance, a considerable reduction in density towards

---

* *Corresponding author.*
E-mail: alexander.kauffmann@kit.edu (A. Kauffmann).

6.2–7 g/cm^3, which is significantly below state-of-the-art Ni-based superalloys, is achieved [1–3]. However, challenges have to be faced regarding the insufficient oxidation behaviour at temperatures below 1000 °C, even when the oxidation-critical phase Mo$_3$Si has been eliminated [2,4]. In contrast, an entirely eutectic Mo–Si–Ti alloy (Mo–20Si–52.8Ti at%) comprising Mo$_{SS}$ solid solution and the intermetallic (Ti,Mo)$_5$Si$_3$ phase exhibits excellent oxidation resistance in the pesting-critical regime at 800 °C [3,5]. It was found that a continuous mixed SiO$_2$–TiO$_2$ scale with a thickness of (9 ± 2) μm was formed after 100 h of cyclic oxidation. The corresponding specific mass change was only about 0.3 mg/cm^2. However, why this alloy does not show any pesting behaviour is still an open question. Estimations of separately considered mass change contributions by oxide scale growth and evaporation at 1200 °C for Mo–Si–Ti alloys have shown that alloys comprising higher Ti contents, especially the eutectic alloy, tend to less evaporation [5]. Therefore, the oxide scale formed on the eutectic alloy is regarded as passivating in Ref. [5]. In this article, the oxidation behaviour of the eutectic alloy will be further evaluated by assessing the role of the microstructural length scale and the influence of the chemical composition of the individual phases. With respect to the identification of the root-causes, which lead to suppression of pesting, a series of alloys with varying nominal Ti content and tailored eutectic-/eutectoid microstructures are studied here.

2. Experimental

The investigated alloys were manufactured by arc-melting using an AM/0.5 device by Edmund Bühler GmbH. The respective elements Mo, Si and Ti were used in bulk form with purities of 99.95%, 99.99% and 99.8%, respectively. The melting procedure was performed in a water-cooled Cu crucible under Ar atmosphere of 600 mbar, which has been established after evacuating to 10^{-4} mbar. In order to reduce oxygen residuals, a Zr lump has been molten previously to the alloy. Homogenous element distribution was established by repeating the melting procedure for five times in combination with flipping the ingot between each melting step. The resulting weight loss was ensured to be less than 0.5 wt%. Specific alloys were subsequently heat-treated in a HRTH tube furnace by Carbolite Gero GmbH & Co. KG under Ar atmosphere at 1300 and 1600 °C.

Oxidation samples were manufactured with dimensions of (5 × 5 × 4) mm^3, by means of electrical discharge machining (EDM). To ensure an appropriate surface finish, the machining marks were removed utilising SiC grit P2500 on all faces of the oxidation samples.

The oxidation experiments were performed cyclically in muffle furnaces (Carbolite Gero and Nabertherm) in laboratory air at 800, 1100 and 1200 °C. Cycle durations varied from 1 to 10 h until 100 h total test duration was reached. After having been cooled down to room temperature after each cycle, the oxidation samples were weighed with a Sartorius balance with a precision of ±1 μg. The initial weight of the oxidation samples was typically in the range of 300–500 mg (depending on the alloy). During the entire oxidation experiments the samples were kept in Al$_2$O$_3$ baskets but were turned around between the cycles.

Sample preparation for microstructural analysis for scanning electron microscopy (SEM) included grinding steps down to SiC grit P2500, 1 and 3 μm polishing steps with diamond suspension. Final polishing was performed using stabilised silica suspension by Buehler. For (scanning) transmission electron microscopy investigations (STEM), thin slices with less than 3 mm in diameter were machined by EDM, ground down to SiC grit P4000 with a thickness in the range of 100 μm and subsequently electrochemically jet-polished. Jet-polishing was performed using a TenuPol-5 by Struers GmbH at room temperature with an electrolyte consisting of H$_2$SO$_4$ and methanol at a ratio of 1:4 and an applied voltage of 15 V.

A D2 Phaser diffraction system by Bruker was used for X-ray diffraction (XRD) measurements in order to determine the crystal structure of the present phases. It was equipped with a Cu tube operating at 30 kV and 10 mA, while the resulting radiation was filtered by Ni foil and detected by a LynxEye line detector operating in 2Θ with a step size of 0.01°. The cubic and hexagonal lattice parameters were determined by applying a Nelson-Riley approach [6] and a modified least square fitting method [7], respectively.

SEM analysis was performed on an EVO 50 and an Auriga 60 system, both provided by Carl Zeiss AG. Both were equipped with energy dispersive X-ray spectroscopy (EDX) systems either by Thermo Fisher Scientific or EDAX. Acceleration voltages of 20 kV for imaging and 8–10 kV for EDX analyses were used, respectively. Besides secondary electron imaging (SE), backscatter electron (BSE) imaging contrast was used in order to characterise the respective phases and microstructures. In accordance to this, EDX measurements were carried out to further characterise the obtained microstructures and oxide scales. Quantitative image analysis included determination of the volume fractions of the present phases and microstructural regions. The respective phases were assigned manually and the corresponding areal fractions were determined by pixel counting. By assuming isotropy and isometry of the microstructures, the gained areal fractions were converted into volume fractions. Additionally, the phase boundary fraction P (see Eq. (1), [8], p. 81) was determined by applying a linear intersection approach to representative BSE images in order to evaluate the fine length scale of the attained microstructures.

$$P = 2\frac{\overline{N}}{L} \tag{1}$$

Thereby, $\overline{N}$ is the number of intersections and L the overall length of the lines. Lamellar spacing was not specified since the binary eutectic microstructures were either both, degenerated and partially lamellar fibrous or homogenously coarsened.

TEM investigations were performed on a Talos F200X of FEI at an acceleration voltage of 200 kV. For scanning transmission microscopy high-angle annular dark-field (STEM-HAADF) imaging a camera length of 95 mm was utilised. The chemical composition was determined using STEM-EDX mappings.

3. Results and discussion

This section is structured as follows: first, the results on the microstructural analyses and the oxidation experiments of the

Table 1 – Microstructural features of the eutectic alloy in ac and ht condition: volume fractions of Mo_{SS} and $(Ti,Mo)_5Si_3$ and phase boundary fraction P.			
Mo–20Si–52.8Ti (at%)	$v^{Mo_{SS}}$ (vol%)	$v^{(Ti,Mo)_5Si_3}$ (vol%)	P (μm^{-1})
eutectic ac	47 ± 2	53 ± 2	0.60 ± 0.04
eutectic ht (1600 °C, 150 h)	50 ± 2	50 ± 2	0.23 ± 0.02

eutectic alloy with different microstructural length scale is presented (Section 3.1). Second, influencing factors like volume fraction of eutectic regions, nominal composition of the alloy and the Ti content in the respective phases are assessed in order to develop a better understanding for the achieved pesting-resistance (Section 3.2). Finally, results on the oxidation behaviour of single-phase bcc Mo_{SS} are shown and correlated to the oxidation behaviour of the Mo–Si–Ti alloys (Section 3.3).

3.1. Microstructural characterisation and study of the oxidation behaviour at 800 and 1200 °C

A previously studied fully eutectic alloy Mo–20Si–52.8Ti (at%) was reported to exhibit a surprisingly good oxidation behaviour even at the critical (pesting) temperature of 800 °C [3]. The good oxidation resistance, especially under pesting conditions, was speculated to be related to the fine-scaled eutectic microstructure consisting of Mo_{SS} and $(Ti,Mo)_5Si_3$ [3]. Short diffusion paths for elements like Si, which form protective oxide scales (e.g. silica), facilitate fast coverage of the surface including less pesting-resistant phases like Mo_{SS}, by oxide scale formation. In other studies, coverage or sealing of surface-near non-protective phases/regions was improved by alloying Mo–Si-based alloys with B leading to the formation of a low-viscous borosilicate layer at higher temperatures (beyond 1000 °C) in the transient stage of oxidation [9–12]. In order to assess the importance of the microstructural length scale for pesting-resistance, the oxidation behaviour of an artificially coarsened eutectic microstructure by an additional heat treatment (ht) is compared to the as-cast (ac) variant. The rapidly cooled ac variant is characterised by a degenerated, locally fibrous fine-scaled microstructure with a phase boundary fraction of (0.60 ± 0.04) μm^{-1} (see Table 1 and Fig. 1a). In contrast, a significantly decreased phase boundary fraction of (0.23 ± 0.02) μm^{-1} is achieved in the ht variant (see Table 1 and Fig. 1b). Both variants comprise Mo_{SS} and $(Ti,Mo)_5Si_3$ at a ratio of about 1:1 (see Table 1). It is not possible to assign the matrix forming phase by 2D pixel connectivity analysis. However, it seems that both phases are present as laterally expanded interconnecting networks (see coloured parts of the micrographs in Fig. 1a and b, respectively). The pixel clusters corresponding to Mo_{SS} are highlighted by "cold" colours of green to blue, whereas the pixel clusters referring to $(Ti,Mo)_5Si_3$ are coloured in "warm" colours of red to yellow. A 3D duplex structure of both phases is likely to be present in both conditions.

Cyclic oxidation experiments reveal comparably good oxidation behaviour in the entire temperature range of 800, 1100 and 1200 °C (see Fig. 1c, data at 1100 °C is omitted due to similarity to 1200 °C). At 800 °C, small specific mass changes of (0.04 ± 0.12) mg/cm^2 in ac and (-0.55 ± 0.04) mg/cm^2 in ht condition are attained after 100 h. At 1200 °C, specific mass changes in the range of (3.1 ± 0.1) mg/cm^2 and (3.8 ± 1.4) mg/cm^2 are observed in the ac and ht condition, respectively. Note the larger scatter of data for the ht variant at 1200 °C.

The corresponding microstructures of the respective oxidised samples are depicted in Fig. 2 (the images at 1100 °C are again omitted due to similarity to the observations made at 1200 °C). When comparing the variants oxidised at 800 °C (see Fig. 2a and b), it can be concluded that: (a) In the ac condition, the fine-scaled eutectic microstructure leads to the formation of a thin oxide scale composed of mixed SiO_2 and TiO_2, as has already been reported elsewhere [3,5]. (b) The coarsened microstructure exhibits a more complex, site-specific oxidation behaviour, being caused by the difference in oxidation rate of the individual phases. This might also be the case in the ac condition. However, the microstructural scale is that fine leading to an intermixing of the oxides formed on the individual phases, which are hard to be distinguished. In the ht variant, this distinction can be revealed by SEM imaging even after 100 h of testing (see Fig. 2b). The oxidation of Mo_{SS} is characterised by rapid formation of TiO_2 with small islands of SiO_2 being embedded inhomogeneously. The coarse Mo_{SS} regions guide the oxidation attack towards the substrate. In contrast, the surface-near $(Ti,Mo)_5Si_3$ regions slowly form a thin top oxide layer being mainly composed of TiO_2 (see BSE contrast and compare to the literature review on the oxidation behaviour of $(Ti,Mo)_5Si_3$ in the paragraph below). However, cracks within the surface-near $(Ti,Mo)_5Si_3$ regions are present. It can be argued whether this cracking is thermally induced due to the cyclic experimental procedure or these cracks have already been present prior to oxidation testing. Since there are significantly less cracks present in the core of the substrate and due to the large anisotropy of the coefficient of thermal expansion (CTE) in Ti_5Si_3 [13,14], thermally induced cracking is likely to occur. Possible inward diffused oxygen does not lead to an increase in thermal anisotropy, but to a rather slight decrease (ratio of linear coefficients of thermal expansion is reduced from $(2.9 \pm 0.7) \times 10^{-6}$ °C^{-1} to $(2.5 \pm 0.3) \times 10^{-6}$ °C^{-1} in $Ti_5Si_3O_{0.4}$) [13]. Additionally, an isothermal oxidation test at 800 °C for 100 h of the ht condition reveals that significantly less cracks are present within the surface-near $(Ti,Mo)_5Si_3$ (see Fig. 2c). Thus, paths for severe oxidation inside these phase regions are avoided. However, despite cracking in $(Ti,Mo)_5Si_3$, the oxidation sample stays intact as TiO_2 formation only occurs along the crack flanks and is inhibited within a small surrounding volume. The cracks are almost located perpendicular to the c-axis of the $(Ti,Mo)_5Si_3$ regions and independently of the orientation of the silicide regions. Thus, direct pathways for oxide formation through their entire length of the $(Ti,Mo)_5Si_3$ regions are not enabled. In accordance with this observation, the inward oxidation progress through Mo_{SS} regions is stopped when $(Ti,Mo)_5Si_3$ regions terminate the respective pathway towards
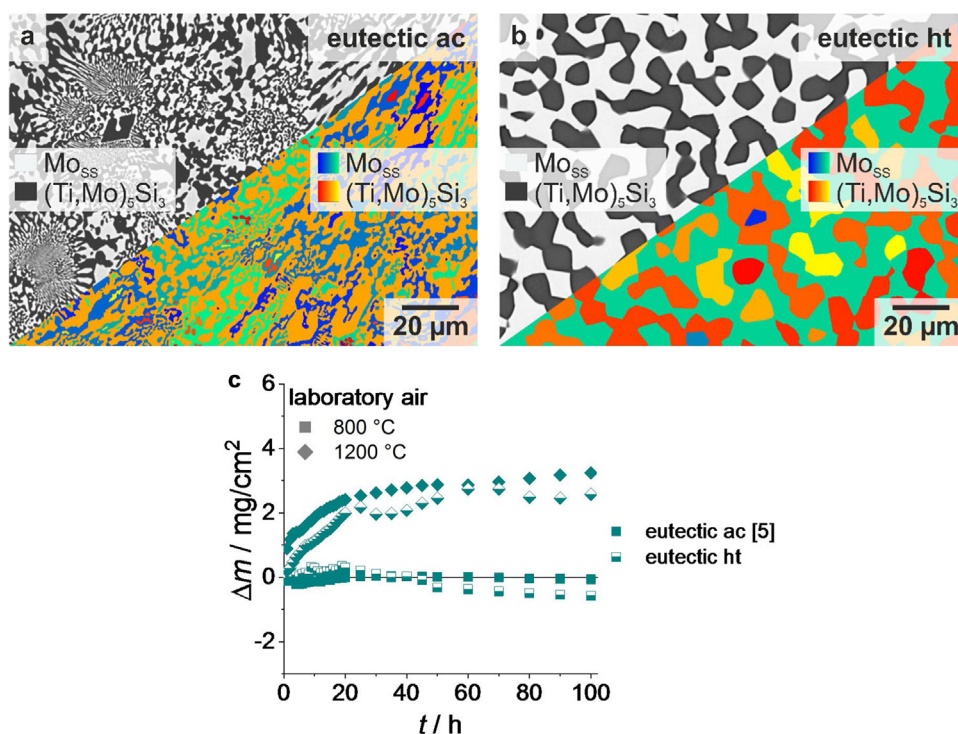
Fig. 1 – BSE micrographs of the microstructure of the eutectic alloy in the ac state (a) and after heat-treatment at 1600 °C for 150 h (b). This includes corresponding coloured microstructures (Mo$_{SS}$ is highlighted by "cold" colours of green to blue and (Ti,Mo)$_5$Si$_3$ by "warm" colours of yellow to red; pixel from single clusters of a phase are the same colour). Exemplary cyclic oxidation experiments at 800 °C (squares) and 1200 °C (diamonds) (c). (For interpretation of the references to color in this figure legend, the reader is referred to the web version of this article.)

the substrate. As there is no matrix character of neither Mo$_{SS}$ nor (Ti,Mo)$_5$Si$_3$, further oxidation in Mo$_{SS}$ or along cracks in (Ti,Mo)$_5$Si$_3$ is at least decelerated: neither critical selective internal oxidation/corrosion (less than 20 μm of internal corrosion after 100 h), nor significant mass losses (−0.5 mg/cm^2 after 100 h) occurred.

The analysis of the oxidation behaviour of a (Ti,Mo)$_5$Si$_3$-based Mo–Si–Ti alloy in Ref. [15] matches the observed oxidation behaviour of the (Ti,Mo)$_5$Si$_3$ regions in the eutectic alloy well. (Ti,Mo)$_5$Si$_3$ is reported to possess a suitable oxidation resistance with a specific mass change of less than 2 mg/cm^2 after 10 h [16] and an oxide scale of less than 10 μm in thickness after isothermal oxidation at 900 °C for 100 h [15]. The oxide scale is characterised by an outer TiO$_2$ scale on top of a duplex oxide scale composed of an SiO$_2$ matrix with finely distributed TiO$_2$ particles [16]. Obviously, the Mo content in (Ti,Mo)$_5$Si$_3$ (being 26.4 at% in Ref. [15]) does not deteriorate the oxidation behaviour of Ti$_5$Si$_3$. The oxidation behaviour of monolithic Ti$_5$Si$_3$ and the effect of interstitials was studied by several authors [17–21]. Besides the amount of O, N and C, it is especially the Si content, which is regarded as being determining for sufficient oxidation behaviour at 1000 °C [19,21]. Ti$_5$Si$_3$ and Ti$_5$Si$_{2.8}$, the latter being deficient in Si content, show accelerated specific mass gain (more than 10 mg/cm^2 and 20 mg/cm^2 after 20 h, respectively) under isothermal oxidation conditions in air at 1000 °C. This is attributed to the crack formation in the thin SiO$_2$ scale which is caused by growing subscales TiN and TiSi$_2$ [19]. In contrast, the Si-enriched

silicide Ti$_5$Si$_{3.2}$ possesses an outstanding oxidation behaviour with less than 3 mg/cm^2 in specific mass change after 50 h at 1000 °C [19] which is attributed to the continuous, passivating SiO$_2$ scale [19,21]. Depending on the Si/Ti ratio, SiO$_2$ or TiO$_2$ is forming as stable oxide [17].

At 1200 °C, the oxide scale morphology of the ac and ht variant is essentially the same. An outer TiO$_2$ layer is observed on top of a SiO$_2$–TiO$_2$ duplex scale (see Fig. 2d and e). The ratio of SiO$_2$ to TiO$_2$ within the duplex scale is close to 1:1 for both conditions. A small amount of porosity of typically less than 1.5 vol% is present within the oxide scale and at the interface of the oxide scale and the substrate for both conditions. Additionally, an internal oxidation zone is observed which is characterised by considerable precipitation in Mo$_{SS}$.

Investigation of the internal oxidation zone by SEM-EDX analyses reveals the presence of Si- and Ti-rich oxide particles within Mo$_{SS}$, as well as Ti-rich oxides along the phase boundaries (see high-resolution SEM-EDX maps for the constituent elements Mo, Si, and Ti and additionally O in Fig. 3a and b). Besides the surface-near oxide particles, homogenously distributed Si- and Ti-rich precipitates are identified within Mo$_{SS}$. These are formed due to the thermal treatment (see Supp. 1) and are likely to originate from a supersaturation of Mo$_{SS}$ in Si and Ti. Supersaturation of the Mo$_{SS}$ is rationalised by fast cooling conditions together with reduced element solubility with decreasing temperature [22–25].

The already discussed striking difference in oxidation behaviour of the individual phases Mo$_{SS}$ and (Ti,Mo)$_5$Si$_3$ is
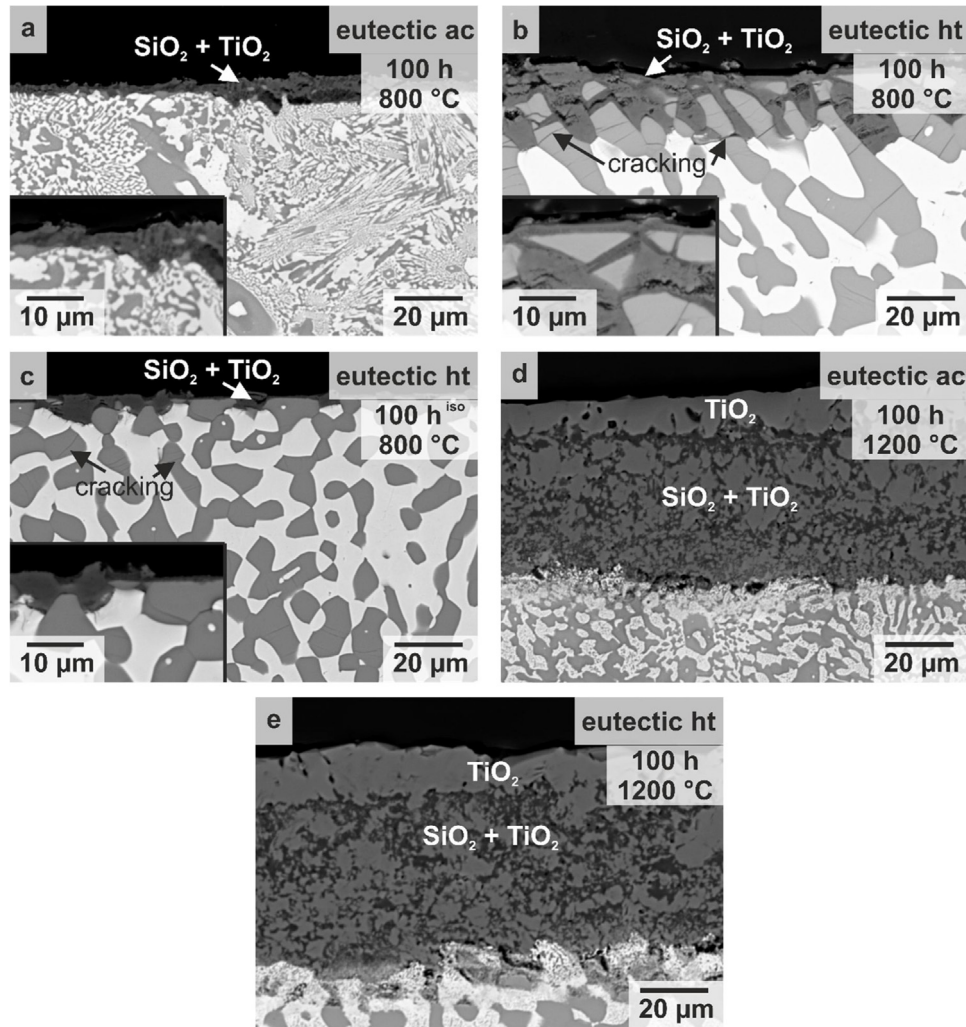
Fig. 2 – BSE micrographs of the cross sections of the cyclically oxidised samples after 100 h at 800 °C of the ac (a) and ht variant (b) in comparison to an isothermally oxidised sample after 100 h of the ht variant (c). BSE micrographs of the oxide scales formed at 1200 °C after 100 h on the ac (d) and ht variant (e).

more pronounced in the coarsened ht variant. This can also be noted when evaluating the oxide scale thicknesses (see Fig. 4), which reveals considerably increased scatter at 800 °C in the ht variant. However, the average values after 100 h have to be regarded as comparable when data scatter is taken into account, namely (5 ± 2) μm in the ac vs. (9 ± 8) μm in the ht variant. The same applies to the observations made at 1200 °C where the resulting oxide scales have comparable thicknesses of (60 ± 13) μm and (48 ± 13) μm in the ac and ht condition, respectively. Note the already mentioned internal oxidation at 1200 °C of approximately 10 μm in the two variants.

The oxidation behaviour of the ac and ht variant is quite similar on a macroscopic level at 800 °C. However, on a microscale, the different oxidation behaviour of the individual phases is revealed to be more prominent in the ht variant, whereas in the ac variant a mutually interacting oxidation behaviour of the respective phases is observed. At 1200 °C, both variants show similar oxide scale morphology along with comparable weight changes. Thus, the sufficient oxidation behaviour of the eutectic alloy (ac and ht vari-

ant) is *not* facilitated by the fine-scaled microstructure. At temperatures below 1000 °C, the otherwise reasonable ability of SiO_2 to cover the substrate surface is restricted due to its considerably increased viscosity [26]. For example, typical Mo–Si-based alloys were still found to undergo pesting, even when alloyed with B to reduce viscosity by the formation of a borosilicate oxide scale [11] or with fine-scaled microstructures down to $1 \, \mu m^{-1}$ and below in phase boundary fraction [4,27,28]. Additionally, TiO_2 is of crystalline nature and, therefore, exhibits non-flowing characteristics in the entire temperature range. In the case of Mo–Si–B alloys, even additional macro-alloying with Ti does not lead to sufficient resistance under pesting conditions [1,2,4]. Conclusively, the achieved pesting-resistance is neither determined by surface-diffusion processes, as the coarsened eutectic microstructure still reveals pesting-stability, nor by viscous oxide scale flow providing coverage of the substrate surface. Thus, chemical conditions are accounted for being responsible for the pesting-resistance, which will be addressed in the following section.
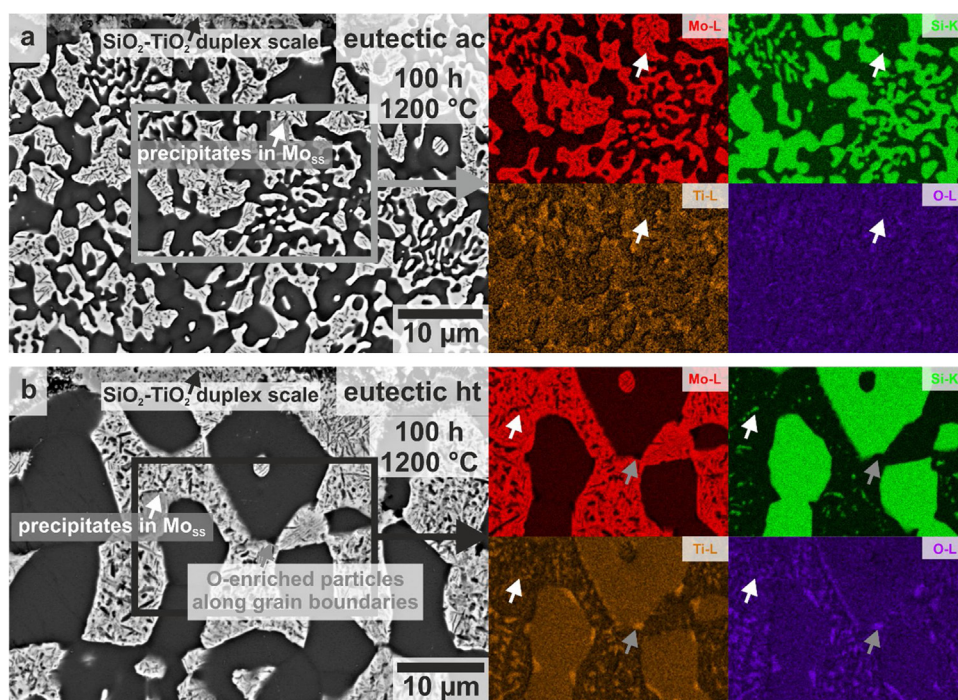
Fig. 3 – BSE micrographs of the internal oxidation zone of the ac (a) and the ht variant (b) subsequent to cyclic oxidation at 1200 °C for 100 h and the corresponding SEM-EDX maps of Mo (red), Si (green), Ti (orange) and O (purple). (For interpretation of the references to color in this figure legend, the reader is referred to the web version of this article.)
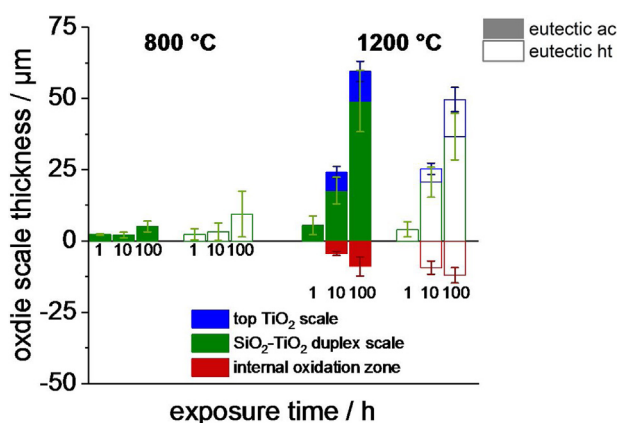

Fig. 4 – Evolution of the oxide scale thickness with test duration at 800 and 1200 °C for for the ac (full bars and the ht variant (open bars), respectively.

3.2. Compositional influencing factors on the pesting-stability

Since we highlighted the importance of the nominal Ti content of the alloy and especially the Ti content of Mo_{SS} for suppression of pesting in our previous paper (Ref. [5], alloy A and B), it is likely that the chemical composition of the individual phases is decisive for an adequate oxidation resistance. Therefore, we focus here on alloys with systematically varying Ti content in the composition range framed by the eutectic alloy, exhibiting good oxidation behaviour at 800 °C, and the eutectoid alloy Mo–21Si–34Ti (see below) suffering from pesting at

800 °C [3]. We included several additional alloys (alloy C1, C2 and D) compared to our previous article. The relevant details of these alloys are summarised in Table 2.

Alloy Mo–21Si–34Ti, resembling the reference alloy with minimum Ti content, possesses a complete eutectoid microstructure of $(Mo,Ti)_5Si_3$ and Mo_{SS} after an appropriate heat-treatment at 1300 °C for 200 h (see Fig. 5a). When increasing the Ti content towards the eutectic alloy, mixed eutectic–eutectoid microstructures are attained. In Fig. 5b and c an example of an intermediate eutectic–eutectoid alloy, alloy B, is shown before and after heat-treatment, respectively. The resulting microstructures are equivalently (or even more) fine-scaled like the eutectic alloy with (1.04 ± 0.05) μm^{-1} in the eutectoid alloy and (0.95 ± 0.07) μm^{-1} in alloy B. However, the additional heat treatment in order to complete the eutectoid decomposition of $(Mo,Ti)_3Si$ is noteworthy which leads to very fine eutectoid regions.

The results of the cyclic oxidation experiments at 800 °C of these alloys are displayed in Fig. 6 revealing a transition in oxidation behaviour. Alloys with nominal Ti contents equal to or higher than 43 at% (compare to alloy A, see also Ref. [5]) do not show any catastrophic oxidation behaviour, whereas for lower nominal Ti contents the severity of pesting is getting more pronounced with decreasing Ti content (see alloys D, B and the eutectoid alloy). The following specific mass changes are observed after 100 h: A ac: (-2.0 ± 0.9) mg/cm^2, C1 ac: (0.2 ± 0.1) mg/cm^2, C2 ac: (-10.0 ± 9.0) mg/cm^2, D ht: (-60.0 ± 1.7) mg/cm^2, B ht: (-120.1 ± 22.0) mg/cm^2, eutectoid: (-167.2 ± 12.3) mg/cm^2.

Conclusively, the oxidation behaviour of the investigated alloys is significantly influenced by their nominal Ti content.

Table 2 – Composition and phase boundary fraction P of the additionally investigated alloys. The listed Ti-rich alloys C2, C1 and A (nominal Ti content 43 at% and higher) are used in ac condition as the eutectoid decomposition was completed during casting, whereas the Ti-lean alloys D, B and the eutectoid alloy are used in ht condition.

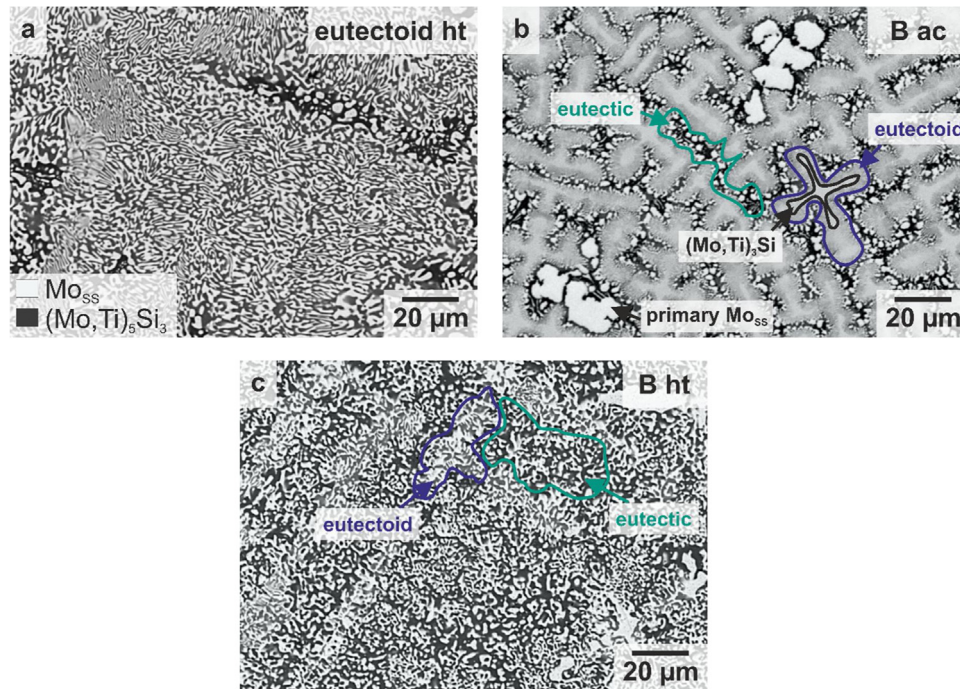| Alloy		Nominal composition (at%)	P (μm^{-1})
Alloy C2		Mo–21Si–47Ti	ac: (0.74 ± 0.18)
Alloy C1	Ti-rich	Mo–21.6Si–44.2Ti	ac: (0.71 ± 0.29)
Alloy A		Mo–21Si–43.4Ti	ac: (0.56 ± 0.14)
Alloy D		Mo–21.5Si–41.5Ti	ht: (0.80 ± 0.09)
Alloy B	Ti-lean	Mo–21Si–38.7Ti	ht: (0.95 ± 0.07)
Eutectoid alloy		Mo–21Si–34Ti	ht: (1.04 ± 0.05)

Fig. 5 – BSE micrographs of the eutectoid alloy in ht condition (a) in comparison to the microstructure of the eutectic–eutectoid alloy B in ac (b) and ht condition (c).
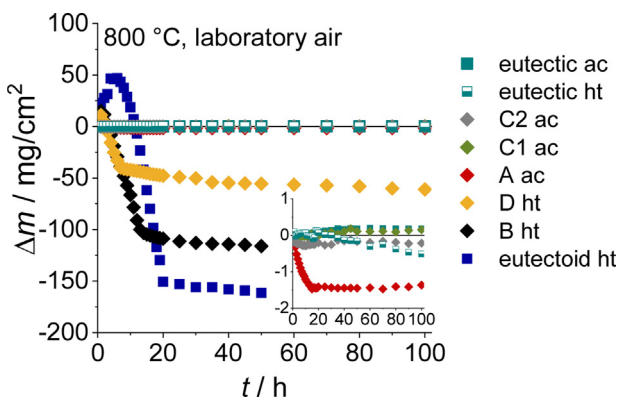

Fig. 6 – Cyclic oxidation experiments of the investigated alloys at 800 °C. Please note that only one representative oxidation curve is displayed for each alloy; while three to five tests were performed in total for each alloy (see Supp. 2).

However, the difference in nominal Ti content results in a shift of the solidification paths, especially leading to different primary solidifying phases (even though in small volume fractions) and whether eutectic or eutectoid microstructures are formed. While the eutectic comprises $(Ti,Mo)_5Si_3$ which is believed to be pesting-resistant like Ti_5Si_3, the eutectoid microstructures contain $(Mo,Ti)_5Si_3$. $(Mo,Ti)_5Si_3$ with 20 and 40 at% Ti are known to be pesting-resistant as well, as was shown by Azim et al. and Burk et al. in Refs. [29,30]. A thin mixed oxide scale comprising SiO_2 as matrix and finely distributed TiO_2 particles is formed on both, the Ti-lean and Ti-rich silicides, whereas the latter is characterised by a reduced oxide scale thickness at higher temperatures [29,30]. However, an underlying internal (oxidation) zone, depleted in Ti with O-enriched grain boundaries and TiO_2 formation at former porous triple points of the grain boundaries is observed [29].

In order to further evaluate the assumption that the oxidation behaviour might be influenced by the chemical composition of the respective phases and microstructures, the local chemical composition of the individual phases and microstructural regions were determined. The eutec-
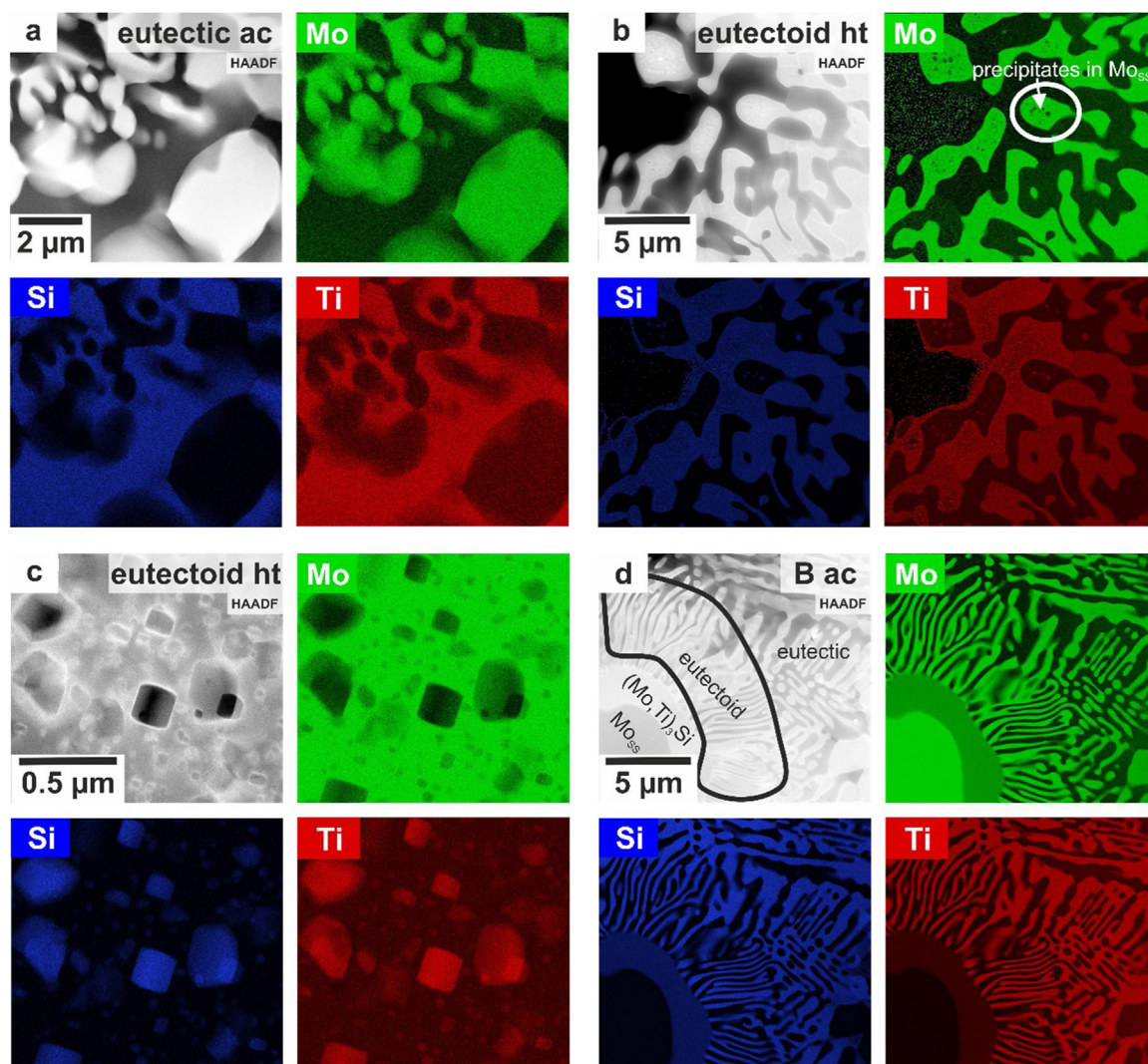
Fig. 7 – HAADF images of the microstructures analysed by STEM-EDX and corresponding STEM-EDX mappings of the respective elements Mo (green), Si (blue), Ti (red) of the eutectic alloy in the ac state (a), the eutectoid alloy in the ht state (precipitates within Mo_{SS} circled in white), including the investigation of the Mo_{SS} region (c), and the eutectic–eutectoid alloy B in the ac state (d). (For interpretation of the references to color in this figure legend, the reader is referred to the web version of this article.)

Alloy	Phase	Mo (at%)	Si (at%)	Ti (at%)
Table 3 – STEM-EDX results of minimum five line scans in the respective areas of the investigated alloys.				
Eutectic alloy ac	Mo_{SS}	58.7 ± 5.3	2.4 ± 0.3	38.9 ± 5.5
	$(Ti,Mo)_5Si_3$	13.3 ± 3.8	23.2 ± 3.0	63.5 ± 4.0
Eutectoid alloy ht	Mo_{SS}	74.1 ± 0.5	2.6 ± 0.3	20.6 ± 0.3
	cuboidal precipitates in Mo_{SS}	16.3 ± 1.4	30.3 ± 0.9	49.5 ± 1.1
	spherical precipitates in Mo_{SS}	59.7 ± 1.6	10.3 ± 0.9	26.7 ± 1.2
	$(Mo,Ti)_5Si_3$	15.5 ± 3.7	29.5 ± 1.7	42.6 ± 2.2
Alloy B ac	Mo_{SS} (eutectic)	69.3 ± 4.1	2.7 ± 0.1	28.0 ± 4.0
	M_5Si_3 (eutectic)	21.2 ± 5.4	24.6 ± 4.3	54.2 ± 1.5
	Mo_{SS} (eutectoid)	69.8 ± 4.3	4.8 ± 2.1	25.5 ± 2.3
	M_5Si_3 (eutectoid)	29.3 ± 7.3	22.8 ± 2.9	47.9 ± 4.9

tic and eutectoid reference alloys and in the intermediate eutectic–eutectoid alloy B were investigated by means of STEM-EDX. The corresponding STEM-EDX mappings are

depicted in Fig. 7. The eutectic and eutectoid reference alloys clearly reveal fine-scaled microstructures composed of Mo_{SS} and silicide regions (see Fig. 7a and b for STEM-EDX results

and Supp. 3a–d for corresponding TEM-SAD diffraction patterns). Moreover, in the eutectoid alloy, cuboidal and spherical precipitates within Mo$_{SS}$ are observed (see Fig. 7b and c). The cuboidal precipitates were found to be Ti- and Si-rich, whereas the spherical precipitates were found to be rich in Mo (see also Table 3). It is likely, that these precipitates formed during subsequent heat-treatment due to supersaturation of the Mo$_{SS}$ achieved by rapid cooling after the arc-melting. The intermediate eutectic–eutectoid alloy B was analysed in the as-cast state for the sake of easier distinction between the eutectic and eutectoid regions. The section of alloy B shown in Fig. 7d, depicts both, eutectic and eutectoid regions. While the eutectoid regions originate from former (Mo,Ti)$_3$Si, the eutectic regions solidify from the residual melt in interdendritic regions. Based on the colour levels of the STEM-EDX mappings, a chemical composition difference in the eutectic and eutectoid regions cannot be recognised. For further analysis, additional line scans were performed as summarised in Table 3.

The focus is especially placed on the site-specific Ti content in Mo$_{SS}$ (Mo$_{SS}$ in eutectic vs. eutectoid regions). The eutectic and eutectoid reference alloys reveal a significant difference in Ti content in Mo$_{SS}$ of namely (38.9 ± 5.5) at% to (20.6 ± 0.3) at%, respectively. In contrast, this difference is considerably diminished in the eutectic and eutectoid regions of the intermediate alloy B. It was found that the Mo$_{SS}$ comprises (25.5 ± 2.3) at% and (28.0 ± 4.0) at% Ti in the eutectoid and eutectic regions, respectively. Additionally, the M$_5$Si$_3$ silicide phases in both, the eutectic and eutectoid regions in alloy B, reveal comparable Ti and Mo contents within the range of scatter. Although, the M$_5$Si$_3$ silicides cannot be assigned to hexagonal Mn$_5$Si$_3$-type D8$_8$ (Ti,Mo)$_5$Si$_3$ or tetragonal W$_5$Si$_3$-type (Mo,Ti)$_5$Si$_3$ solely by these chemical compositions, it is likely that the Mo-leaner M$_5$Si$_3$ phase is the hexagonal (Ti,Mo)$_5$Si$_3$ phase, as XRD measurements confirmed (see Supp. 4). However, the transition from hexagonal (Ti,Mo)$_5$Si$_3$ to tetragonal (Mo,Ti)$_5$Si$_3$ still remains under debate, as for instance, in alloy Mo–40Ti–30Si a Mo content of 26.4 at% was reported in hexagonal (Ti,Mo)$_5$Si$_3$ which resembled the major phase [15]. The thermodynamic pseudobinary (Ti,Mo)$_5$Si$_3$ – (Mo,Ti)$_5$Si$_3$ system calculated by Bondar and Lukas in Ref. [31] assumes the existence of a two-phase region of (Ti,Mo)$_5$Si$_3$ and (Mo,Ti)$_5$Si$_3$ when the Mo content in (Ti,Mo)$_5$Si$_3$ exceeds approximately 18 at% at temperatures near the liquidus. With decreasing temperature, a decreasing Mo content solved in (Ti,Mo)$_5$Si$_3$ is predicted. Yang et al. concluded in Ref. [32], based on an isothermal section at 1600 °C, the maximum Mo content in (Ti,Mo)$_5$Si$_3$ to be 12.5 at% and the maximum Ti content in (Mo,Ti)$_5$Si$_3$ to be 40 at%. The evaluation of the TEM diffraction pattern of the M$_5$Si$_3$ silicides in alloy B only provided further verification within the eutectic region (see Supp. 3e) as the hexagonal (Ti,Mo)$_5$Si$_3$ D8$_8$ crystal structure was ascertained. In contrast, within the fine-structured eutectoid regions unambiguous identification of the crystal structure was not possible.

The following graph (see Fig. 8) displays the volume fraction of the respective phases/regions of the investigated alloys in accordance with the nominal Ti content and the global vs. local Ti content in Mo$_{SS}$. Generally, the volume fraction of eutectic microstructure is decreasing with decreasing Ti content. However, among the intermediate eutectic–eutectoid
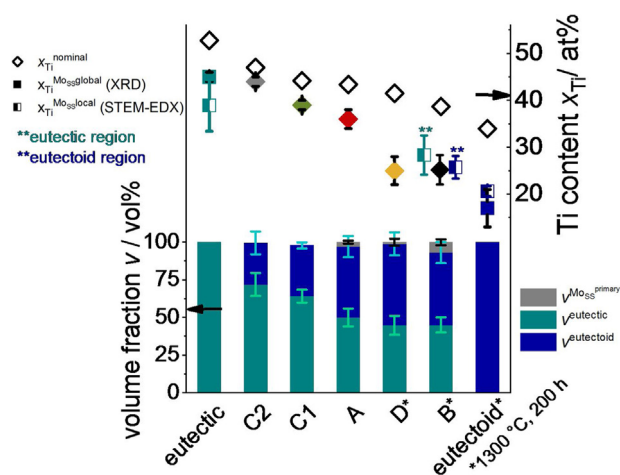

Fig. 8 – Nominal Ti content vs. globally determined Ti content (by means of XRD) and local Ti content (by means of STEM-EDX) of all investigated alloys in correlation with the volume fractions of the respective phases/microstructural regions.

alloys A, B and D, the volume fraction of the eutectic is similar within the scatter of data. Therefore, it is obvious that the volume fraction of the eutectic does not have an influence on the oxidation behaviour, as alloy A is pesting-resistant, while alloy D is not. Nevertheless, the difference in Ti content in Mo$_{SS}$ (correlated to the nominal Ti content) is prominent throughout all alloys and the threshold of Ti in Mo$_{SS}$ for suppression of pesting, assumed in our previous paper [5], is confirmed to be 35 at%.

3.3. Investigation of the oxidation behaviour of Mo$_{SS}$

In order to verify the influence of the Ti content in Mo$_{SS}$ on the oxidation behaviour, almost single-phase bcc Mo$_{SS}$ alloys with Ti contents varying from 20 to 50 at% were oxidised in air at 800 °C. Thereby, alloy Mo–20Ti resembles the 'worst case' scenario of the composition of Mo$_{SS}$, whereas alloy Mo–40Ti–3Si (Si partially enriched along the grain boundaries) represents the assumed promising composition with a high Ti content and considerable Si content within the investigated Mo–Si–Ti alloy series. The observed mass change in dependence of test duration at 800 °C is plotted in Fig. 9a . Although all Mo$_{SS}$ alloys suffer from severe pesting, it is clearly demonstrated that the oxidation rate is significantly reduced with increasing Ti content, as alloy Mo–20Ti oxidises with −33 (mg/cm^2)/h and alloy Mo–50Ti with −14 (mg/cm^2)/h, respectively. Moreover, if Mo$_{SS}$ contains Si, the oxidation rate is further retarded as is revealed by comparing alloy Mo–40Ti to alloy Mo–40Ti–3Si with a reduction in the oxidation rate from −19 (mg/cm^2)/h to −14 (mg/cm^2)/h (Mo–40Ti–3Si). Additionally, the initially observed peak in weight gain decreases from 62 mg/cm^2 (Mo–40Ti) to 32 mg/cm^2 (Mo–40Ti–3Si). This initial weight gain is likely to be caused by the formation of solid Ti-rich oxides, which might be crack-free during the first few oxidation cycles. Ongoing cyclic thermal impact might lead to cracking of the Ti-rich oxides, which then allows accelerated oxide formation of volatile MoO$_3$ and consequent rapid mass
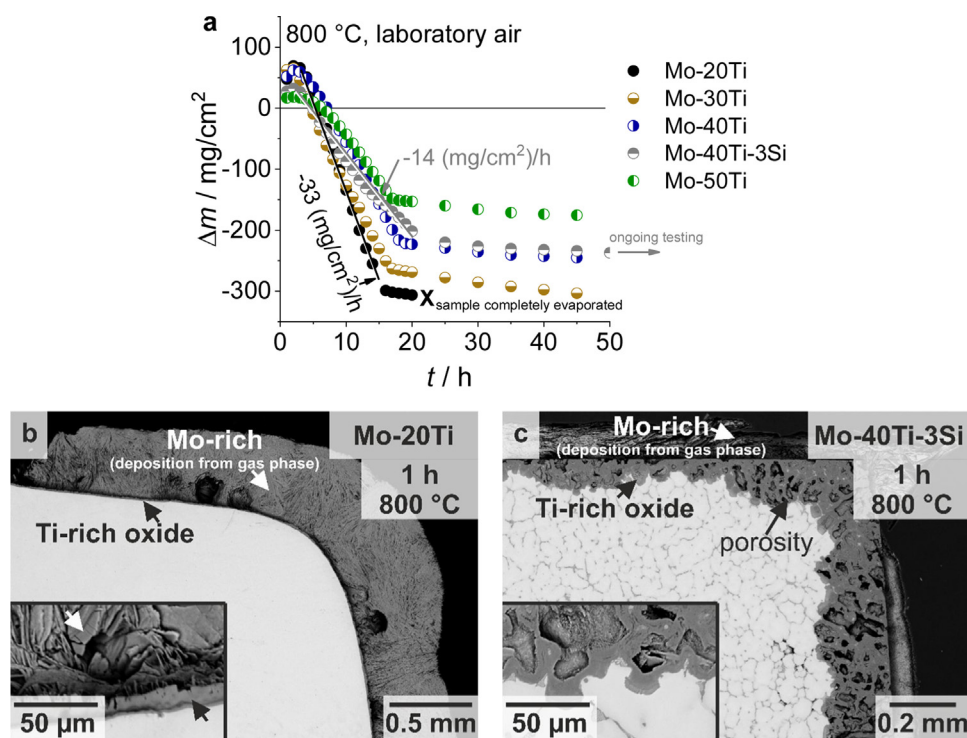
Fig. 9 – Results of the cyclic oxidation experiments in air at 800 °C for selected Mo$_{SS}$ alloys: mass change in dependence of test duration for one representative sample for each alloy (three samples were tested in total) (a), BSE micrographs of the oxidised samples after 1 h of alloy Mo-20Ti (b) and alloy Mo-40Ti-3Si (c).

loss. Additionally, the Ti-rich and Si-containing Mo$_{SS}$ does not disintegrate and the mass change stabilises after approximately 20 h. In contrast, the Mo$_{SS}$ alloy with only 20 at% Ti is completely evaporated after 15 h. This is already seen in the BSE micrographs of the oxidised samples after 1 h shown in Fig. 9b and c. Mo–20Ti oxidises to volatile MoO$_3$ which partially re-deposits on the sample revealed by the less-adherent, needle-shaped Mo-rich oxide covering the sample discontinuously (highlighted by white arrows in Fig. 9b). It is clearly seen that the substrate is significantly consumed during 1 h of oxidation. At the substrate–air interface (below the re-deposited Mo-rich oxide scale), a less than 10 µm thick Ti-rich oxide scale is observed (highlighted by black arrows in Fig. 9b). In contrast, alloy Mo–40Ti–3Si oxidises by inwardly growing, solid Ti-rich oxides which are highly porous (highlighted by black arrows in Fig. 9c), likely caused by the simultaneous evaporation of MoO$_3$ which also re-deposits moderately on the oxidised surface (highlighted by white arrows in Fig. 9c). However, the sample stays intact and the former substrate surface is still recognised as such. The Si-enriched regions along the grain boundaries do not exhibit specific oxidation characteristics. However, formation of pores possibly due to MoO$_3$ evaporation is observed along the grain boundaries.

The catastrophic oxidation behaviour of pure Mo is known to be caused by the formation of volatile MoO$_3$ at temperatures of 500 °C and above [33]. In the case of Mo–Si alloys, monolithic MoSi$_2$ with 66 at% Si only exhibits pesting-resistance under certain circumstances (density >95%, crack-free [33,34]), otherwise complete disintegration at 500 °C is reported [35–37]. Several authors argue that local stresses, being caused by the

volume expansion due to local oxidation along pre-existing cracks or grain boundaries, lead to cracking and disintegration of the substrate [36–38]. Thereby, oxidation of Mo to MoO$_3$ leads to a volume expansion of 340% and oxidation of Si to solid SiO$_2$ yields a volume expansion of up to 180% [36]. Pesting was found to be suppressed when alloying Mo(Si,X)$_2$ with Al, Ti or Zr [38]. The suppression of pesting is attributed to the higher affinity of the additional alloying elements to oxygen compared to Si and to the formation of oxides with a lower volume expansion than that of (pure) SiO$_2$ [38]. In general, the pesting phenomenon is influenced by the chemical composition, impurities and the microstructure including its defects [34,39]. The oxidation behaviour of Mo–Ti alloys has not been reported so far. The present investigations on Ti-containing Mo$_{SS}$ indicate that there is no pesting-resistance for up to 50 at% Ti, but significant reduction of MoO$_3$ evaporation is achieved with increasing Ti content. The available data on Mo–Si–O equilibria at temperatures around 800 °C is described in detail in Ref. [41]. In contrast, only a small fraction of the isothermal Mo–Ti–O section for high Ti-contents is reported so far [42,43]. However, it is assumed that the fraction of equilibrium MoO$_3$ is reduced for the same O partial pressure and similar Si or Ti contents when comparing Mo–Si and Mo–Ti alloys. Therefore, the disturbance of oxide scale formation by evaporation might be less pronounced in high Ti-containing Mo$_{SS}$.

For comparison, M$_5$Si$_3$ silicides (M = Mo or Ti, or both) reveal pesting-stability. Thus, hexagonal (Ti,Mo)$_5$Si$_3$ comprising 34.7 at% Ti and considerable amounts of Mo (26.4 at%) exhibits pesting resistance [15], as well as the tetragonal

$(Mo,Ti)_5Si_3$ containing 23 at% Mo and 40 at% Ti [30]. Although monolithic Ti-/Mo-containing M_5Si_3 silicides were shown to be pesting-resistant [15,30], the alloys investigated in the present work only comprise 50 vol% silicide phases. Conclusively, the superposition of the pesting-resistance of the $(Ti,Mo)_5Si_3$ and the considerably reduced evaporation of MoO_3 in high-Ti containing Mo_{SS} results in the observed threshold of 43 at% nominal Ti for pesting stability.

4. Summary and conclusion

The eutectic Mo–Si–Ti alloy Mo–20Si–52.8Ti shows unexpected outstanding oxidation behaviour even at 800 °C where typically pesting is observed in all other Mo(-Si)-based alloys [4,10,40]. The fine-scaled microstructure composed of Mo_{SS} and $(Ti,Mo)_5Si_3$ leads to formation of a very thin mixed SiO_2–TiO_2 oxide scale upon cyclic exposure to 800 °C for 100 h. While nearly single-phase $(Ti,Mo)_5Si_3$ was shown to be pesting-resistant by forming a SiO_2 and TiO_2 containing oxide scale in Refs. [15,16], single-phase bcc Mo_{SS} undergoes rapid oxidation by forming volatile MoO_3. This is likely due to the high Mo concentration and the resulting high Mo activity. Thereby, Ti-rich Mo_{SS} exhibits less severe pesting behaviour due to the formation of TiO_2 preventing complete consumption of the substrate by evaporation of MoO_3. Nonetheless, the eutectic alloy does not suffer from significant mass loss, which accounts for the assumption that MoO_3 formation is less dominant. This is in good agreement with the evaluation of Obert et al. [5] where the individual contributions of mass loss due to MoO_3 formation and mass gain due to solid oxide formation by oxidation of Ti and Si to the overall mass change were addressed. However, the fine-scaled microstructure was found not to be mandatory in order to achieve an adequate oxidation resistance, as an artificially coarsened, globular microstructure exhibits comparable specific mass change without detectable volatilisation of the Mo_{SS} regions. Nonetheless, preferred selective inward oxidation of Mo_{SS} is observed, while on top of the $(Ti,Mo)_5Si_3$ regions an outer thin TiO_2 scale is formed. Oxidation testing of eutectic–eutectoid alloy series with systematic variation of the eutectic volume fraction showed that also this fraction is not decisive whether pesting can be suppressed or not. Alloy A and D with approximately 50 vol% eutectic exhibited an adequate oxidation resistance and suffered from pesting, respectively. With the aid of the chemical composition of the respective phases, it was revealed that the nominal Ti content and particularly the Ti content in Mo_{SS} is determining the oxidation resistance. With a minimum of 35 at% Ti in Mo_{SS}, pesting-resistance is achieved in the multi-phase alloy. Thereby, the variation of the local Ti content in Mo_{SS} in eutectic and eutectoid regions of intermediate eutectic–eutectoid alloys was found to be within the scatter of data. Conclusively, this article reveals the microstructural and chemical requirements for pesting-resistance. It is a combined effect of the oxidation-resistant $(Ti,Mo)_5Si_3$ phase and the Ti-rich Mo_{SS}, which is less prone to volatilisation. As the formed oxide scales are multi-phase with complex morphologies, a detailed discussion of the oxidation kinetics requests both, consideration of mass changes and thickness evaluation. This includes nanoscale analyses on the influential factors on the prevalent kinetics, which is beyond the scope of this article, but will be addressed in a future study.

Conflict of interest

Prime novelty statement

Acknowledgements

Appendix A. Supplementary data

Supplementary material related to this article can be found, in the online version, at https://doi.org/10.1016/ j.jmrt.2020.06.002.

REFERENCES

[1] Azim MA, Schliephake D, Hochmuth C, Gorr B, Christ H-J, Glatzel U, et al. Creep resistance and oxidation behavior of novel Mo-Si-B-Ti alloys. JOM 2015;67(11):2621–8.

[2] Azim MA, Burk S, Gorr B, Christ H-J, Schliephake D, Heilmaier M, et al. Effect of Ti (macro-) alloying on the high-temperature oxidation behavior of ternary Mo–Si–B alloys at 820–1300 °C. Oxid Met 2013;80(3–4):231–42.

[3] Schliephake D, Kauffmann A, Cong X, Gombola C, Azim MA, Gorr B, et al. Constitution, oxidation and creep of eutectic and eutectoid Mo-Si-Ti alloys. Intermetallics 2019;104:133–42.

[4] Schliephake D, Azim MA, Klinski-Wetzel KV, Gorr B, Christ H-J, Bei H, et al. High-temperature creep and oxidation behavior of Mo-Si-B alloys with high Ti contents. Metall Mater Trans A 2014;45(3):1102–11.

[5] Obert S, Kauffmann A, Heilmaier M. Characterisation of the oxidation and creep behaviour of novel Mo-Si-Ti alloys. Acta Mater 2020;184:132–42.

[6] Nelson JB, Riley DP. An experimental investigation of extrapolation methods in the derivation of accurate unit-cell dimensions of crystals. Proc Phys Soc 1945;57(3):160–77.

[7] Tsai DS, Hsu SE, Hung MP. A simple method for the determination of lattice parameters from powder X-ray diffraction data. Mater Trans JIM 1989;30(7):474–9.

[8] Kurzydlowski KJ, Ralph B. The quantitative description of the microstructure of materials, vol. 3. Boca Raton: CRC Press; 1995.

[9] Meyer M, Kramer M, Akinc M. Boron-doped molybdenum silicides. Adv Mater 1996;8(1):85–8.

[10] Meyer MK, Thom AJ, Akinc M. Oxide scale formation and isothermal oxidation behavior of Mo–Si–B intermetallics at 600–1000 °C. Intermetallics 1999;7(2):153–62.

[11] Yan MF, MacChesney JB, Nagel SR, Rhodes WW. Sintering of optical wave-guide glasses. J Mater Sci 1980;15(6):1371–8.

[12] Yoshimi K, Nakatani S, Suda T, Hanada S, Habazaki H. Oxidation behavior of Mo_5SiB_2-based alloy at elevated temperatures. Intermetallics 2002;10(5):407–14.

[13] Williams JJ, Kramer MJ, Akinc M. Thermal expansion of Ti_5Si_3 with Ge, B, C, N, or O additions. J Mater Res 2000;15(8):1780–5.

[14] Zhang L, Wu J. Thermal expansion and elastic moduli of the silicide based intermetallic alloys $Ti_5Si_3(X)$ and Nb_5Si_3. Scr Mater 1998;38(2):307–13.

[15] Majumdar S, Singh PK, Pandey AK, Rao GVSN. Kinetics of oxide scale growth on a $(Ti,Mo)_5Si_3$ based oxidation resistant Mo-Ti-Si alloy at 900–1300 °C. High Temp Mater Process 2019;38:533–40.

[16] Majumdar S, Paul B, Singh PK, Kishor J, Kain V. Effect of Si content on microstructure, mechanical and oxidation properties of hot pressed Mo-Ti-Si alloys. Intermetallics 2018;100:126–35.

[17] Rahmel A, Spencer PJ. Thermodynamic aspects of TiAl and $TiSi_2$ oxidation: the Al-Ti-O and Si-Ti-O phase diagrams. Oxid Met 1991;35(1–2):53–68.

[18] Tang Z, Thom AJ, Akinc M. Role of nitrogen on the oxidative stability of Ti_5Si_3 based alloys at elevated temperature. Intermetallics 2006;14(5):537–43.

[19] Tang Z, Williams JJ, Thom AJ, Akinc M. High temperature oxidation behavior of Ti_5Si_3-based intermetallics. Intermetallics 2008;16(9):1118–24.

[20] Taniguchi S, Minamida T, Shibata T. Oxidation behaviour of Ti_5Si_3 at temperatures between 1400 and 1700 K. In: Materials science forum. Trans Tech Publications; 1997.

[21] Williams JJ, Akinc M. Oxidation resistance of Ti_5Si_3 and $Ti_5Si_3Z_x$ at 1000 °C (Z = C, N, or O). Oxid Met 2002;58(1–2):57–71.

[22] Gokhale AB, Abbaschian GJ. The Mo-Si (molybdenum-silicon) system. J Phase Equilib 1991;12(4):493–8.

[23] Murray JL. The Mo-Ti (molybdenum– titanium) system. Bull Alloy Phase Diagr 1981;2(2):185–92.

[24] Kieffer R, Cerwenka E. Beitrag zum System Molybdän Silizium. Zeitschrift für Metallkunde 1952;43(4):101–5.

[25] Perepezko JH, Sakidja R, Kim S, Dong Z, Park JS. Multiphase microstructures and stability in high temperature Mo-Si-B alloys. In: Third international symposium on structural intermetallics. 2002.

[26] Hetherington G. The viscosity of vitreous silica. Phys Chem Glasses 1964;5(5):130–6.

[27] Burk S, Gorr B, Krüger M, Heilmaier M, Christ H-J. Oxidation behavior of Mo-Si-B-(X) alloys: macro-and microalloying (X = Cr, Zr, La_2O_3). JOM 2011;63(12):32–6.

[28] Rioult FA, Imhoff SD, Sakidja R, Perepezko JH. Transient oxidation of Mo–Si–B alloys: effect of the microstructure size scale. Acta Mater 2009;57(15):4600–13.

[29] Azim MA, Gorr B, Christ H-J, Lenchuk O, Albe K, Schliephake D, et al. Effect of Ti content and nitrogen on the high-temperature oxidation behavior of $(Mo, Ti)_5Si_3$. Intermetallics 2017;90:103–12.

[30] Burk S, Gorr B, Christ H-J, Schliephake D, Heilmaier M, Hochmuth C, et al. High-temperature oxidation behaviour of a single-phase $(Mo, Ti)_5Si_3$ (Mo–Si–Ti) alloy. Scr Mater 2012;66(5):223–6.

[31] Bondar A, Lukas H-L. In: Effenberg G, Ilyenko S, editors. Molybdenum–silicon–titanium, in light metal systems: Part 4. Berlin, Heidelberg: Springer-Verlag; 2006. p. 385–405.

[32] Yang Y, Chang YA, Tan L, Du Y. Experimental investigation and thermodynamic descriptions of the Mo–Si–Ti system. Mater Sci Eng A 2003;361(1–2):281–93.

[33] Gulbransen EA, Andrew KF, Brassart FA. Oxidation of molybdenum 550–1700 °C. J Electrochem Soc 1963;110(9):952–9.

[34] Meschter PJ. Low-temperature oxidation of molybdenum disilicide. Metall Trans A 1992;23(6):1763–72.

[35] Berztiss DA, Cerchiara RR, Gulbransen EA, Pettit FS, Meier GH. Oxidation of $MoSi_2$ and comparison with other silicide materials. Mater Sci Eng A 1992;155(1–2):165–81.

[36] Grabke HJ, Meier GH. Accelerated oxidation, internal oxidation, intergranular oxidation, and pesting of intermetallic compounds. Oxid Met 1995;44(1–2):147–76.

[37] McKamey CG, Tortorelli PF, DeVan JH, Carmichael CA. A study of pest oxidation in polycrystalline $MoSi_2$. J Mater Res 1992;7(10):2747–55.

[38] Yanagihara K, Maruyama T, Nagata K. Effect of third elements on the pesting suppression of Mo-Si-X intermetallics (X = Al, Ta, Ti, Zr and Y). Intermetallics 1996;4. p. 133-S139.

[39] Berkowitz-Mattuck JB, Dils RR. High-temperature oxidation: II. Molybdenum silicides. J Electrochem Soc 1965;112(6):583–9.

[40] Supatarawanich V, Johnson DR, Liu CCT. Effects of microstructure on the oxidation behavior of multiphase Mo–Si–B alloys. Mater Sci Eng A 2003;344(1–2):328–39.

[41] Beyers R. Thermodynamic considerations in refractory metal-silicon-oxygen systems. J Appl Phys 1984;56(1):147–52.

[42] English JJ. Binary and ternary phase diagrams of columbium, molybdenum, tantalum, and tungsten. Ohio: DMIC report; 1961. p. 156–7.

[43] Farrar PA, Stone LP, Margolin H. Titanium-molybdenum-oxygen system. J Met 1956;8:595–600.